Highly Active and Stable Catalysts of Phytic Acid-Derivative Transition Metal Phosphides for Full Water Splitting

Gong Zhang,[†,⊥] Guichang Wang,[∥] Yang Liu,[§] Huijuan Liu,*,[†,⊥] Jiuhui Qu,[‡,⊥] and Jinghong Li*,[§]

[†]State Key Laboratory of Environmental Aquatic Chemistry, and [‡]Key Laboratory of Drinking Water Science and Technology, Research Center for Eco-Environmental Sciences, Chinese Academy of Sciences, Beijing 100085, China

[§]Department of Chemistry, Key Laboratory of Bioorganic Phosphorus Chemistry & Chemical Biology, Beijing Key Laboratory for Microanalytical Methods and Instrumentation, Tsinghua University, Beijing 100084, China

[∥]Department of Chemistry, Key Laboratory of Advanced Energy Materials Chemistry (Ministry of Education) and Collaborative Innovation Center of Chemical Science and Engineering (Tianjin), Nankai University, Tianjin 300071, China

[⊥]University of Chinese Academy of Sciences, Beijing 100039, China

S *Supporting Information*

ABSTRACT: Application of transition metal phosphide (TMP) catalysts for full water splitting has great potential to help relieve the energy crisis. Various methods have been investigated to obtain high catalytic activity, but the use of electronic structure regulation by incorporation of different elements is of particular simplicity and significance for development of a universal TMP synthesis method. We herein describe a novel approach for fabricating a series of TMPs by pyrolyzing phytic acid (PA) cross-linked metal complexes. The introduction of oxygen atoms into TMPs not only enhanced their intrinsic electrical conductivity, facilitating electron transfer, but activated active sites via elongating the M−P bond, favoring the hydrogen evolution reaction (HER) or oxygen evolution reaction (OER). MoP exhibited relative low HER overpotentials of 118 mV and 93 mV while supporting a current density of 20 mA·cm^{-2} in 0.5 M H_2SO_4 and 1 M KOH electrolytes, respectively. When CoP was applied as a catalyst for OER, only 280 mV overpotential was required to reach current density of 10 mA·cm^{-2}. Additionally, PA-containing precursors enabled intimate embedding of TMPs onto a flexible substrate surface (carbon cloth), so that electron injection from substrate and transport to the active sites was facilitated. Remarkably, an alkaline electrolyzer was able to achieve a current density of 40 mA·cm^{-2} at the low voltage of 1.6 V, demonstrating its potential for practical overall water splitting without the use of noble metals.
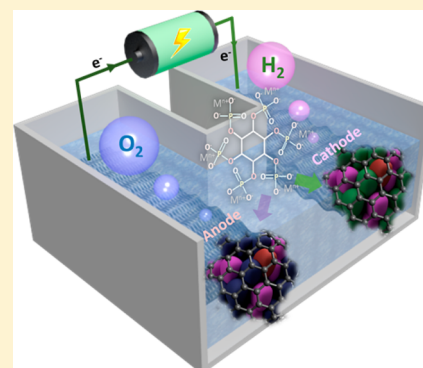
INTRODUCTION

Production of hydrogen (H_2) via electrolytic water-splitting has been considered as a key alternative to the traditional fuels (coal, oil, and natural gas).[1,2] The electrochemical production of hydrogen is hampered by the following limitation: lack of effective replacements for noble-metal-based materials, which are still the best known catalysts to reduce overpotentials of the two half-reactions (hydrogen evolution reaction (HER) and oxygen evolution reaction (OER)) in full water-splitting reaction. Notably, Pt-based catalysts are considered as state-of-the-art for the HER,[3] while Ir and Ru oxides are the benchmark electrocatalysts for the OER.[4] Therefore, it is highly imperative to develop new electrocatalysts with both superior properties and low cost. A number of alternatives including non-noble metal,[5] metal composites,[6] and metal-free electro-catalysts[7] have been recently investigated as potential substitutes for noble-metal catalysts.

During recent years, considerable efforts have been made to clarify the catalytic mechanism for the transition metal phosphides (TMPs) for the purpose of achieving excellent electrocatalytic performance.[8−10] Some former theoretical and experimental studies have concluded that the catalytic activity for the HER arises from metal sites located on the surface.[11] In TMPs (M = Mo, Ni, Co, Fe, etc.), the concentration of M is diluted due to the existence of P atoms, and the formation of M−P bonds seems to have a negligible effect on the electronic properties of the metal species.[12] However, the M−P bonds not only induce a weak "ligand effect" that enables a high activity for the dissociation of molecular hydrogen but also provide moderate bonding to trap catalytic intermediates to prevent the deactivation of the catalysts.[13] Once the metal sites have been occupied, the adsorbates (H^+/H_2O) prefer to interact with M−P bridge sites, where the electron transfer to a bridging proton was determined to be the rate-determining step (RDS) for the whole HER process. This suggests that the M−P bond length could be a reasonable reactivity descriptor. As the M−P bond length increases, greater electron localization will be facilitated

on the P sites and thus reduce the barrier for bonding to the adsorbates.

Moreover, the elongation of the M–P bond can also accelerate the oxidation process of metal atoms at high overpotential. Formation of a TMP/MO_x core–shell assembly is key for a high OER activity, in which the TMP core plays a significant role as a conductive support in providing an effective electron pathway to the active MO_x shell.[14] However, limited intrinsic conductivity impedes transport of electrons from electrode to catalyst, so that additional potential is required to overcome the energy barriers.[15,16] Numerous works have recently reported that it is possible to enhance the electron mobility by doping with other elements, including both metal and nonmetal elements.[17,18] By means of oxygen incorporation, Xie and co-workers reported an optimized MoS_2 catalyst with superior activity for the HER.[19] An important implication of this report is that the introduction of foreign elements indeed provides the opportunity to modulate the intrinsic conductivity and change the electronic structure of the electrocatalyst.

Taking inspiration from these beneficial changes induced by elemental substitution, we here attempted to synthesize a series of nanosized O-doped TMPs by pyrolyzing phytic acid (PA) cross-linked complexes for full water splitting. The naturally ecofriendly and renewable biological compound PA (*myo*-inositol 1,2,3,4,5,6-hexakisphosphate, Figure S1) was considered to be a suitable precursor, in which six phosphate groups can not only provide a P source but can readily cross-link the metal precursors. The incorporation of a small amount of oxygen into TMP was certainly confirmed by physical characterizations. On the basis of a combination of experimental results and theoretical calculations, the oxygen incorporation was determined as one of the decisive factors for superior electrocatalytic activities, which can not only elongate M–P bonds but can promote the intrinsic conductivities in TMP. Additionally, because of two drawbacks present in bulk transition-metal-based catalysts, namely low density of active sites and poor stability, the graphene sheets were simultaneously introduced as a structured support.[20] MoP produced exhibited low HER overpotentials of 118 mV and 93 mV at a current density of 20 mA·cm⁻² in 0.5 M H_2SO_4 and 1 M KOH electrolytes, respectively. When CoP was applied as a catalyst for OER, a 280 mV overpotential was required to achieve a current density of 10 mA·cm⁻². In addition, the PA-complexed precursor was able to firmly bond to a carbon cloth surface, so that an alkaline electrolyzer that achieved a current of 40 mA·cm⁻² at a voltage of 1.6 V was constructed by using TMPs@CC as electrodes.

■ RESULTS AND DISCUSSION

The two TMPs (MoP, CoP) were successfully prepared by calcining product from a solution-based reaction, where metal compounds and PA were used as precursors. As shown in Scheme 1, metal-containing precursors were first chelated with PA molecules via an impregnation method in water–ethanol solution, and the as-formed complexes were meanwhile bonded with functional groups on graphene oxide (GO) (step I). After heating precursors in H_2 (step II), TMP nucleation was highly dispersed on the GO surface, which was eventually converted to RGO under reduction atmosphere. Due to confinement provided by the GO sheets, the growth of TMP crystals was restricted in that area, resulting in nanosized particles embedded in the layered graphene. The samples were structurally characterized by X-ray diffraction (XRD). As

Scheme 1. Synthesis Process for TMP@RGO by Pyrolyzing Phytic Acid Cross-Linked Complexes
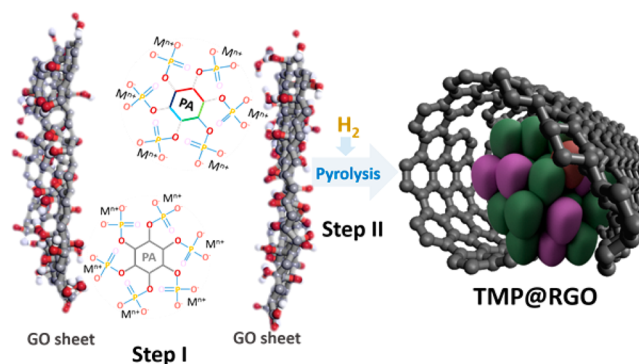
depicted at the top of Figure 1a, the diffraction peaks of the samples could be well indexed to the hexagonal MoP (space
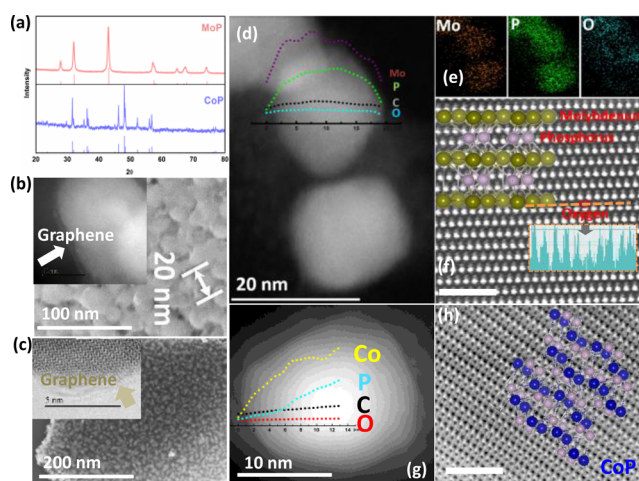

Figure 1. Characterization of TMP samples. (a) XRD patterns and (b, c) SEM images of MoP@RGO and CoP@RGO. (d) STEM image of MoP nanoparticle. Inset: intensities for different elements. (e) Large area STEM-EDS mapping to panel d. (f) HAADF-STEM image of MoP with the corresponding crystal structure superimposed. The intensity profile along the orange dashed line directly shows the presence of O atoms. (g) The STEM image of CoP. Inset: the intensities of the elements present in particles. (h) HAADF-STEM image of CoP with the crystal structure superimposed. Scan bars, 1 nm.

group: $P\bar{6}m2$; $a = b = 3.222$ Å; $c = 3.191$ Å), and orthorhombic CoP (space group: *Pnma*; $a = 5.077$ Å, $b = 3.281$ Å, and $c = 5.587$ Å) (Figure 1a bottom) structures, respectively.

To obtain information on the morphology and structure of the as-synthesized TMPs, detailed microscopic characterizations were performed. According to the results of scanning electron microscopy (SEM) and transmission electron microscopy (TEM), TMP nanoparticles with a diameter around 20 nm were clearly surrounded by layered RGO (Figure 1b,c). The substantial numbers of hydroxyl groups on the GO surface served as nucleation sites after coupling the metal precursors, and the as-formed RGO sheets subsequently encapsulated the as-formed nanoparticles during the reduction process. A control experiment in the absence of GO sheets induced the TMP aggregates (Figure S2), indicating that encapsulation by RGO effectively restricted the growth of TMP particles.

Furthermore, the high-resolution TEM (HRTEM) and aberration-corrected scanning transmission electron microscopy (STEM) images were then analyzed in great detail to investigate atomic models for the TMP NPs. Energy-dispersive X-ray (EDX) spectra (Figure 1d,e) analysis confirmed the MoP@RGO hybrid structure with Mo, P, O, and C as principal elemental components, in good agreement with X-ray photoelectron spectrometry (XPS) results (Figure S3). The intensities of signals for Mo, P, and a small amount of O were limited to the area of the particle, whereas C was present in the entire area (Figure 1d inset). Moreover, the subsequent inspection of resolved high-angle annular dark field (HAADF) images of MoP provided some important clues to the structure. In HAADF images (Figure 1f), bright spots corresponding to Mo atomic columns with the highest atomic number ($Z = 42$), the intermediate-brightness spots representing P ($Z = 15$) atoms, and weak spots probably representing O ($Z = 8$) atoms can be observed in the MoP crystal. The high-resolution TEM image demonstrates the presence of [001]-oriented orthorhombic CoP, and the STEM image reveals the presence of a small amount of oxygen, in all likelihood, in CoP NPs (Figure 1g,h).

To assess electrocatalytic performance, catalyst-based thin films were prepared on glassy carbon (GC) electrodes for cyclic voltammetry in 0.5 M H_2SO_4 and 1 M KOH electrolytes. To remove the emerging bubbles, the working electrode was rotated (1600 rpm) during the measurements. In the acidic electrolyte, a reductive sweep of MoP@RGO hybrid showed a low overpotential (η) of 10 mV for the HER (Figure 2a).
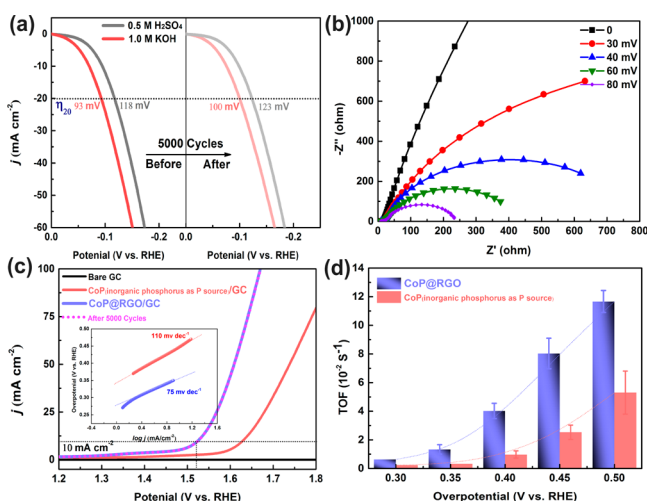

Figure 2. (a) Polarization curves of MoP measured both in 0.5 M H_2SO_4 and 1 M KOH (left) and curves after 5000 potential sweeps at 20 mV·s^{-1} (right), without iR-drop corrections. (b) Nyquist plots at different η values of MoP on glass carbon electrode (GCE). (c) Polarization curves in 1 M KOH with different forms of CoP as catalysts, and curve (dashed line) after 5000 potential sweeps at 20 mV·s^{-1}. (d) TOFs with respect to Co atoms of CoP (inorganic phosphorus as P source) and CoP@RGO hybrid (PA as P source) at different η values.

Afterward, a sharply increased cathodic current was observed when the η value increased beyond 10 mV, corresponding to abundant catalytic H_2 evolution. Meanwhile, in the absence of GO, the MoP aggregates exhibited inferior HER activity, while much lower HER catalytic activity was observed in T-MoP (inorganic phosphorus was used as P resource) with the same

catalyst loading of ~0.28 mg·cm^{-2} (Figure S4). At high current densities (such as 20 mA·cm^{-2} with η of 118 mV), MoP@RGO shows high efficiency relative to other comparable noble-metal-free HER catalysts.[21−23] The HER kinetics of the catalysts were then measured by analyzing Tafel plots (log $j \sim \eta$). The Tafel slope confirms that the HER proceeds via a Volmer−Heyrovsky mechanism. A Tafel slope of ~58 mV·decade^{-1} was measured for MoP@RGO, which was lower than the value of ~76 mV·decade^{-1} for the MoP catalyst and that of 105 mV·decade^{-1} for T-MoP. In KOH solution, the cathodic current for HER increased rapidly starting from a smaller η; only a 93 mV overpotential was required to drive the current density of 20 mA·cm^{-2}. Moreover, the stability was investigated by continuous cyclic voltammetry (CV) on glassy carbon substrate at a constant scanning rate of 20 mV·s^{-1} for 5000 cycles both in 0.5 M H_2SO_4 and 1 M KOH. Only subtle differences were observed in the polarization curves after 5000 cycles, suggesting stability of the catalyst in the long-term electrochemical process.

Electrochemical impedance spectroscopy (EIS) analysis was then performed on MoP catalysts. Consistent with previous studies on Mo-based catalysts, EIS Nyquist plots of the MoP electrodes exhibit behavior characterized by two time constants (Figure 2b). The impedance model for the material consists of a series of resistances: the one in the high frequency region is related to surface porosity (Cd2-R_p); the other at low frequency depends on overpotential (Cd1-R_{ct}), reflecting the charge transfer process during the electrochemical reaction.[24,25] Nyquist profiles of MoP were investigated over a range of overpotentials (0−80 mV), and the constants were fitted by an equivalent electrical circuit with two constant-phase elements. Figure S5 presents low-frequency charge transfer resistance (R_{ct}) and constant-phase element (CPE) as a function of HER overpotential. The calculated values of R_{ct} decreased from 3049 Ω at 0 mV to 184 Ω at 80 mV, indicating that the charge transfer kinetics were significantly accelerated upon η increasing. Meanwhile, the applications of high η increased the double layer capacitance, from 2.63 mF·cm^{-2} at 0 mV to 7.49 mF·cm^{-2} at 40 mV. However, due to the generation of fresh hydrogen species at more negative η, the double layer capacitance promptly decreased to 0.17 mF·cm^{-2} at 80 mV. Nyquist profiles collected at η = 80 mV on various MoP electrodes are listed in Table S1. MoP@RGO electrode exhibited a lower charge transfer impedance value than that for the bulk MoP, in good agreement with the different HER activities. The exchange current density (j_0) of MoP catalysts, an inherent measure of HER activity, was also deduced from the Tafel plots. The j_0 of 2.01 × 10^{-1} mA·cm^{-2} in MoP@RGO was higher than the values of 1.05 × 10^{-1} mA·cm^{-2} and 1.86 × 10^{-2} mA·cm^{-2} for MoP and T-MoP. The electrochemical surface area (ECSA) was next evaluated for further insight into the different catalytic performances. ECSA is proportional to double-layer capacitance (C_{dl}), which can be calculated from different scan rate cyclic voltammograms (CV) (Figure S6a−c).[26,27] C_{dl} values of MoP and T-MoP were 8.05 mF·cm^{-2} and 0.61 mF·cm^{-2}, respectively, almost 2 and 25 times less than a value of 15.30 mF·cm^{-2} presented by MoP@RGO in 0.5 M H_2SO_4 (Figure S6d). A higher ECSA in MoP@RGO indicated that a rapid charge transfer between active sites and electrolyte was achieved. Due to effective dissolution of surface oxides (HER inert species), an abundance of new active sites on the MoP@RGO surface was thereby exposed for the HER in KOH solution, resulting in the slightly higher catalytic performance

than under acid conditions. An increased C_{dl} value of 16.67 mF· cm^{-2} was therefore noticed in 1 M KOH (Figure S7).[28]

To study the OER activity, the electrochemical measurement of CoP was carried out at a loading of 0.28 mg·cm^{-2} on a GC electrode. In contrast to CoP phosphatized by inorganic phosphorus (NaH$_2$PO$_2$), the polarization curve for CoP@RGO hybrid in linear sweep voltammetry (LSV) exhibited a much higher current and earlier onset of catalytic current (Figure 2c). Meanwhile, a η of 280 mV could support a 10 mA·cm^{-2} current density for CoP@RGO, significantly lower than the 400 mV for the CoP comparison electrode and even for other CoP-based forms reported in recent publications.[29,30] As η increased, the catalyst displayed a larger electrocatalytic reaction current, with 100 mA·cm^{-2} at an overpotential of 440 mV, which was almost 4 times higher than that of the contrasted one. Meanwhile, to a part of current density that can possibly result from oxidation of RGO, RGO-400 and RGO-650 were prepared via directly reducing GO with H$_2$ at temperatures of 400 °C and 650 °C. RGO-400 exhibited an obvious oxidation current before water oxidation (1.23 V vs RHE), while the subtle current observed in RGO-650 was mainly due to the non-Faradaic current (Figure S8).[31] The comparison of Raman and FTIR spectra before and after linear sweep voltammetry (from 0.6 to 1.23 V vs RHE) in 1.0 M KOH showed that RGO-650 with lower I_D/I_G possessed thermodynamic stability better than that of RGO-400 (Figure S9). Similarly, PA-GO mixture calcined under 650 °C that we applied here showed no current before the water oxidation potential. Furthermore, observations of previous research have confirmed that the OER is catalyzed by Co and that the presence of a suitable amount of Fe can alter their oxidation state sites, thereby a concurrent increase in OER activity.[32,33] Around 14 μg of Fe was identified in the CoP precursor using inductively coupled plasma mass spectrometry (ICP-Ms) (Figures S10 and S11), the amount of which was not sufficient to alter OER activity. The anodic current was proportional to oxygen yield, and thus the higher current density obtained here demonstrated the prominent oxygen evolution behavior of the catalyst.[34] To gain insight into this oxygen evolution activity, Tafel plots of the catalysts were further investigated. The Tafel slope for CoP@RGO was 75 mV·dec^{-1}, much smaller than 110 mV·dec^{-1} measured for the aggregate material. For testing the durability of the catalyst, continuous potential cycling was performed and no perceptible variation was observed between two LSV polarization curves measured before and after 5000 CV cycles, indicating the excellent stability of the hybrid material. To learn more about reaction dynamics during the OER process, the gas generation was further quantitatively measured using gas chromatography (GC) analysis in the anode compartment of the electrolytic cell. The electrolysis was conducted by maintaining a CoP@RGO-loaded anode at 1.60 V vs RHE for 240 min. Faradaic efficiency (FE) was therefore determined from the difference between theoretical calculation and experimental measurement. In addition to molecular O$_2$, no other volatile products were detected during the OER process, and the subtle difference (FE approximated to 98%) between the two values mainly resulted from oxidation of the Co center (Figure S12). Moreover, turnover frequencies (TOFs) for each active site were further estimated via the following function,[35]

$$\text{TOF} = (J \times A)/(4 \times F \times n) \tag{1}$$

where J is current density at a given overpotential, A is surface area of electrode, 4 represents 4 electrons·mol^{-1} of O$_2$, F is

Faraday constant, and n is number of moles of metal in the electrode. We first assumed that all of the Co ions are catalytically active and thereby calculated their TOFs. However, because some metal sites are indeed inaccessible in the OER reaction, the calculated TOFs represent a lower limit.[36] Much higher TOFs were estimated for the CoP@RGO hybrid under different η values (Figure 2d). At η = 500 mV, TOF of the hybrid was 0.12 s^{-1}, more than 4 times higher than that of the contrasted one.

Good catalytic performance of the PA-derivative TMPs aroused our curiosity as to the chemical structure of the catalysts. Extended X-ray absorption fine structure spectroscopy (EXAFS) measurements were first performed to investigate the arrangement of atoms around the photoabsorbers (Mo, Co). The Mo K-edge oscillation curves for two PA-derivative MoPs exhibit remarkable differences in contrast to the T-MoP, indicating different atomic arrangements (Figure 3a inset). The
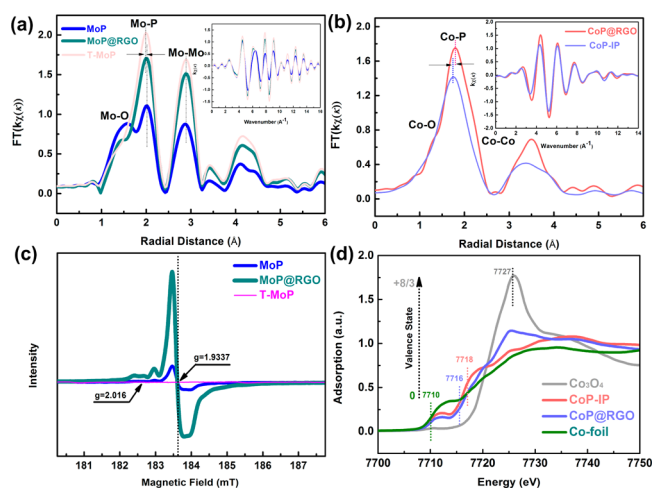

Figure 3. Mo (a) and Co (b) K-edge extended XAFS oscillation function $k^3[\chi(k)]$ (inset) and their corresponding Fourier transform (FT) (k is wave vector, $\chi(k)$ = oscillation as a function of photoelectron wavenumber). (c) Room temperature (273 K) EPR measurements for various MoP catalysts. (d) X-ray absorption near-edge structure (XANES) analysis of Co-based compounds. Note: IP is an abbreviation for inorganic phosphorus.

Fourier transform (FT) curves present some peaks ranging from 1 to 4 Å, corresponding to Mo−Mo and Mo−P coordination in all MoP samples. However, new peaks at 1.40−1.60 Å corresponding to Mo−O coordination were observed in PA-derivative MoP, in good agreement with the HAADF image. Compared with T-MoP, diffraction peaks in MoP@RGO slightly shifted to lower degrees, which possibly resulted from the lattice expansion by O incorporation (Figure S13). Additionally, Mo−P peak intensities significantly decreased in the presence of Mo−O coordination, which was due to missing atoms in the Mo coordination sphere. Mo−O, Mo−P, and Mo−Mo pairs were then fitted in real space (Figure S14). According to XRD results, a crystal structure with P-$m2$ space group was applied to generate the initial structure for EXAFS analysis in the fitting. In this model, the photoabsorber Mo atom was surrounded by P atoms and Mo atoms as the first and second shells. Fit for T-MoP showed the coordination numbers of 4.83 and 5.28 for P shell and Mo shell, almost the same as for the model (Table S2). However, the fits for PA-derivative MoPs showed that the coordination number

of the P shell decreased to 4.4 and 2.8 for MoP@RGO and MoP, respectively. The missing atoms in the Mo sphere were compensated by the O shells (coordination number of 0.4 and 1.3), whereby the Mo−P distance increased by 0.02 and 0.03 Å, respectively. According to DFT calculation, the bond length of Mo−P was 2.476 Å for pure MoP after optimization, while the bond length increased to 2.82 Å with the introduction of O atoms. The reason may be due to the strong interaction between O and Mo, thus weakening the bonding strength of Mo−P based on the principle of bond order conservation.

In the temperature-programmed reduction process, the metal-containing precursor was first reduced to metal particles, followed by phosphatization to TMPs. The P−O bond is strong, and its reduction requires higher temperatures than that for metal ions. However, active H atoms with high reducing ability will be easily formed by dissociation of H_2 by the as-formed metal particles, which is available to break the P−O bond. The reductive H atoms can spill over to the phosphate and reduce it to phosphorus or phosphine, and the product can readily react with metal particles to form metal phosphide. In contrast to inorganic phosphate, the *myo*-inositol hexakisphosphate structure is conducive to breaking the P−O bond; thereby a small amount of the M−O bonds can be reserved during the TMP formation process. Similarly, the Co K-edge oscillation curve and FT $k^3[\chi(k)]$ functions in R space for CoP@RGO exhibited obvious differences in comparison with the contrasted one (Figure 3b). FT curves present peaks ranging from 1 to 3 Å, corresponding to Co−P and Co−Co, with new Co−O coordination appearing around 1.3 Å, respectively. The FT curve of the contrasted CoP exhibited Co−P coordination with a peak at 1.75 Å, while the peak shifted to 1.81 Å in the PA-derivative CoP@RGO, which resulted from the coordinative unsaturation or surface structural disorder in the presence of O atoms.[37] The Co−P distance increased from 2.21 to 2.23 Å, which was also due to the strong interaction between O and metal atom.

Obviously, the small charge transfer resistance observed would be primarily related to the synergistic effect between TMP crystallites and RGO, which facilitates electron transfer from the electrode to catalyst. On the other hand, it should be noted that the incorporation of the oxygen atom into MPs has the potential to regulate electronic structure and therefore tune their intrinsic conductivities.[38] For example, molybdenum dioxide $(Mo(IV)O_2)$ is a classical metallic material with high electrical conductivity.[39] From the EPR spectrum, the absence of paramagnetic signals indicated that only Mo(III) was present in T-MoP (Figure 3c).[40−42] In contrast, prominent paramagnetic species signals at $g = 1.937$ were observed in the spectrum of PA-derivative MoPs. According to the negligible EPR signal in PA@RGO and up-shifted Mo 3d peaks in the high resolution XPS scan (Figure S15), we confirmed that the paramagnetic centers were due to the presence of Mo(VI), which should be the partial coordination of Mo with O atoms. Moreover, the EPR signal intensity for MoP@RGO was about 6 times more intense than that of bulk materials in the absence of GO, which gave solid evidence that the limited particle diameter (20 nm) in the presence of RGO could enhance the number of catalytically active sites. As depicted in Figure 3d, due to the presence of O atoms, the observed low edge position (7716 eV) in the first-order derivatives of Co−K XANES implied a richness of Co species with a low valence state in CoP@RGO.

First-principle calculations were then carried out to study the effect of O doping. Our theoretical investigations revealed that TMP (M = Mo, Co) showed metallic behavior, with a high density of states (DOS) at the Fermi level, indicating the high microscopic conductivity (Figure S16).[43] After O doping, the metal atoms neighboring the O atom exhibited increased DOS across the Fermi level in contrast to the residual ones (Figure 4); therefore, O-doped TMPs can achieve a much higher DOS
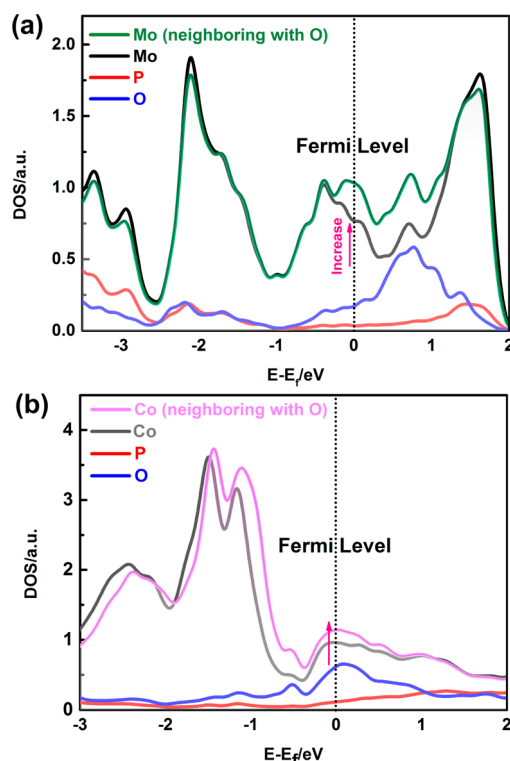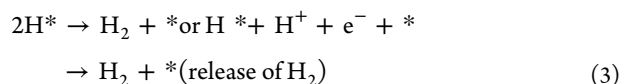

Figure 4. Average density of electronic states of different atoms in (a) O-doped MoP and (b) O-doped CoP.

across the Fermi level, indicating enhanced intrinsic conductivity. Meanwhile, the substituted O atoms increased the electron concentration especially in the conduction band, further facilitating the charge carrier transfer during the electrocatalytic process.[44]

The Gibbs free energy for hydrogen adsorption on the surface of a catalyst is considered to be a reasonable indicator of HER activity.[45] In acid solution, the HER reaction path is mainly composed of proton adsorption and reduction on the surface to form H_{ads}, followed by H_2 formation and desorption, which can be divided into two steps:

$$H^+ + e^- + * \rightarrow H*(\text{hydrogen bonded to catalyst}) \qquad (2)$$

$$2H* \rightarrow H_2 + * \text{ or } H * + H^+ + e^- + *$$
$$\rightarrow H_2 + *(\text{release of } H_2) \qquad (3)$$

where * denotes an active site on the surface. As the binding energy of H atoms plays a key role in determining the overall HER catalytic activity, only the first step was investigated here. Ideal HER activity should be achieved at a value of $\Delta G \approx 0$. Lower ΔG causes a high surface coverage of hydrogen atoms (H_{ads}), while a higher value indicates that the protons bond weakly on the electrocatalyst surface, both of which bring about slow HER kinetics.[46] Table S3 gives the calculated binding

energy and Gibbs free energy at single H coverage on various MoP models. It was found that the H atom tends to bind with a P atom on a surface site. After the introduction of oxygen atoms into MoP, the P binding site is still the optimal site, but the H atom binding energy is slightly reduced compared to that on pure MoP (from −0.83 to −0.68 eV). On the basis of the most stable adsorption site for H atom, the Gibbs free energy was evaluated for the reaction at various H coverages. As depicted in Figure 5, the Gibbs free energy for pure MoP
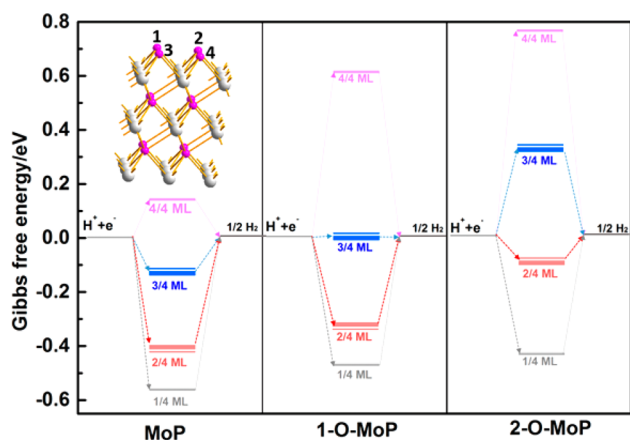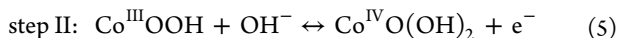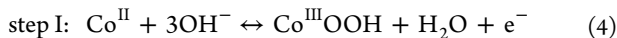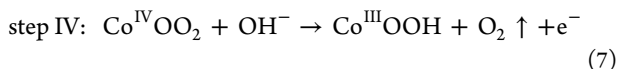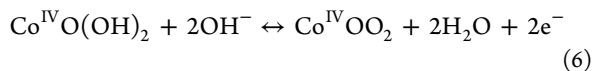

Figure 5. Free energy versus the reaction coordinate of HER for various MoP models (1O−P−MoP and 2O−P−MoP mean that one oxygen or two oxygen atoms are substituted for P into the MoP model). Silver and pink indicate Mo and P atoms, respectively. Our calculation model was designed with four P atoms on the first layer (inset); H coverage can therefore be changed from 1/4 ML to 4/4 ML.

system is a slightly far away from zero energy level. Strikingly, O-doped MoP displays higher HER catalytic activity due to the Gibbs free energy being nearly zero at 3/4 ML for 1O−P−MoP or 2/4 ML for 2O−P−MoP systems. O-doped MoP shows a unique activity because the presence of O elongated the Mo−P bond length, primarily reducing the proton binding barrier for the MoP. Furthermore, a strong binding strength between the catalyst surface and atomic H would slow down the HER due to the difficult desorption of H_2 product. An optimal HER kinetic in the O-doped MoP was achieved when the H binding energy was weakened via increasing Mo−P bond length and thereby promoting the catalytic activity eventually.

Mechanistic studies have proposed that OER on Co-based catalysts in an alkaline electrolyte involves four consecutive steps and can be depicted as follows:[47]

$$\text{step I:} \quad Co^{II} + 3OH^- \leftrightarrow Co^{III}OOH + H_2O + e^- \quad (4)$$

$$\text{step II:} \quad Co^{III}OOH + OH^- \leftrightarrow Co^{IV}O(OH)_2 + e^- \quad (5)$$

step III:

$$Co^{IV}O(OH)_2 + 2OH^- \leftrightarrow Co^{IV}OO_2 + 2H_2O + 2e^- \quad (6)$$

$$\text{step IV:} \quad Co^{IV}OO_2 + OH^- \rightarrow Co^{III}OOH + O_2 \uparrow + e^- \quad (7)$$

Steps I, II, and III are reversible and determine the OER rate, while step IV is fast and irreversible. A similar OER mechanism takes place on our CoP. Co atoms on the surface were first partially oxidized into CoOOH and form the CoP/CoOOH

core−shell assemblies as the actual surface-active sites,[48] which was evidenced not only by Co^{II}-to-Co^{III} oxidation peak around 1.1 V vs RHE in cyclic voltammetry results (Figure 6) but also
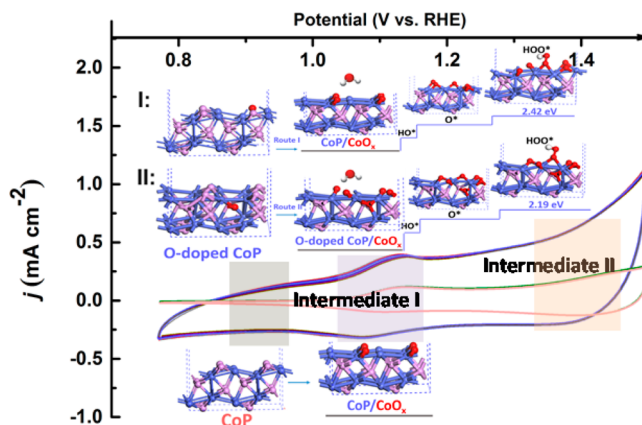

Figure 6. Cyclic voltammetry (CV) responses of O-doped CoP (blue line) and pure CoP (red line) in N_2-saturated 1 M KOH. Catalyst loading was 0.028 mg·cm^{-2}. Scan rate was 20 mV·s^{-1}. Inset shows the reaction Gibbs free energy for the OER on CoP (calculated energies are displayed in Å and eV). Blue, purple, red, and white indicate Co, P, O, and H atoms, respectively.

by the changed P chemical state after CV cycles (Figure S17).[49,50] Intermediate I, including the CoO_x/CoP (route I: surface doping) and CoO_x/O-doped CoP (route II: subsurface doping), was possibly involved during the O-doped CoP transformation at a high potential. The introduction of O element shifted the electron localization to the P sites via elongation of the Co−P bond length (Figure S18), facilitating the conversion of Co to active Co^{III} species. The calculated formation energies of 1.33 and 1.52 eV in routes I and II, respectively, were much less than the value of 1.62 eV in the undoped one. The enhanced conductivity conferred by O doping meanwhile reduced the barrier for electron transport between electrode and catalyst, also contributing to its high ECSA (Figure S19). In the OER process, Co^{III} species (step I) acted as an initiator, and the other key process (step II) was related to the reversible interconversion between Co^{III} and Co^{IV} (intermediate II). In good agreement with the TOF results, much higher amounts of active sites in O-doped CoP can be directly observed by comparing the Co^{III}-to-Co^{IV} oxidation peak around 1.4 V vs RHE. The calculated adsorption energy of *OOH on CoO_x/CoP was 2.42 eV, while it decreased to 2.19 eV in the CoO_x/O-doped CoP system, implying a facile formation of *OOH after O incorporation.

Furthermore, in consideration of its unique properties, it is reasonable to speculate that the PA-cross-linked complex should be a promising precursor that can readily bond to various substrates, which provides a significant potential for scalable application of highly efficient TMP electrocatalysts. The nanoparticles are commonly loaded on the substrates with high intrinsic conductivity,[51,52] among which carbon cloth (CC) is the best choice due to the tunable structures, low cost, and strong tolerance to acid/alkaline environments.[53] The CC surface was first mildly oxidized to create abundant functional groups to promote its interaction with the PA-containing complex, so that the CC surface can be conformally coated by the PA-containing precursor via chemical bonding between phosphoric acid groups in PA molecules and functional groups

on the CC surface (Figure S20). Subsequent pyrolysis led to the formation of TMPs/CC. Meanwhile, a low I_D/I_G value in Raman spectra clearly confirmed the emergence of high degree graphitized carbon after pyrolyzing the PA solution (Figure S21). The high degree graphitized carbon not only enhanced the electrical conductivity but also strengthened the cohesion for TMPs onto CC, whereby electron injection from the substrate and transport to the active sites were further facilitated. According to the SEM images in Figure 7a−d, the changes in roughness on the CC surface were due to the firmly embedded catalysts.
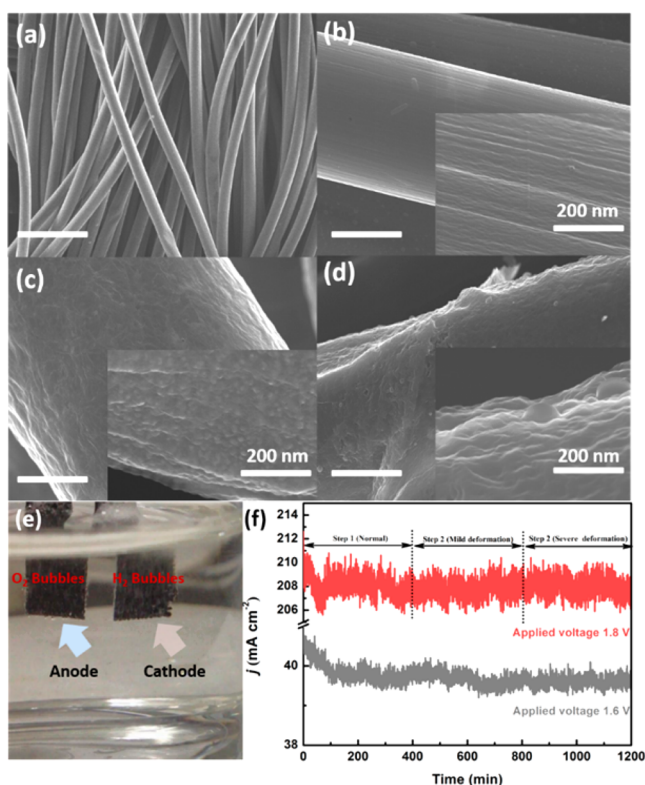

Figure 7. (a, b) SEM images of the carbon cloth. (c, d) SEM images of MoP- and CoP-loaded carbon cloth, respectively. (e) Optical photograph showing the generation of bubbles on the MoP- and CoP-based electrodes. (f) Chronoamperometric measurement of overall water splitting at 1.6 and 1.8 V applied potential across the electrodes. Inset: variation of the current during the deformation, which was divided into mild and severe deformations. After two deformations, only subtle differences compared to the initial measurements were observed.

A water splitting configuration was then devised using MoP/CC and CoP/CC as the anode and cathode in 1.0 M KOH, respectively. Long-term stability of the electrodes was assayed by means of chronoamperometry measurement ($j \sim t$) (Figure 7f). The configuration was able to maintain stable current densities of 40 mA·cm^{-2} and 210 mA·cm^{-2} for 20 h at constant applied biases of 1.6 and 1.8 V, respectively. Additionally, the stability of the electrodes at high current density was exhibited in full water splitting at 1.8 V applied potential with vigorous gas (H$_2$/O$_2$) evolution on the electrodes (Figure 7e). Furthermore, the activity of flexible TMPs/CC electrodes was investigated after deformation of the CC electrode to varying degrees. After two deformation steps, steady current nearly as high as that for the pristine electrode was outputted, revealing

that the electrodes are flexible and can have considerable potential for application applied in harsh environments.

CONCLUSIONS

In summary, we have reported a universal and scalable method to prepare highly active TMP electrocatalysts for full water splitting by pyrolyzing phytic acid cross-linked metal complexes. Moderate introduction of O atoms into the TMPs enhanced their intrinsic conductivities and elongated the M−P bonds, facilitating electron transfer to active sites for catalyzing the HER or OER. The MoP catalyst exhibited low HER overpotentials of 118 mV and 93 mV at a current density of 20 mA·cm^{-2} in 0.5 M H$_2$SO$_4$ and 1 M KOH electrolytes, respectively. Only 280 mV overpotential was required to achieve a current density of 10 mA·cm^{-2} when CoP was applied as the catalyst for the OER. We further firmly embedded PA-derivative TMP electrocatalysts onto a flexible substrate (carbon cloth) in a one-pot process to achieve an electrolyzer, which exhibited remarkably high current densities under relatively low voltage (1.6 V voltage can drive the current density of 40 mA·cm^{-2}). Thus, in view of the energy crisis nowadays, these active O-doped TMP-loaded electrodes have the potential to be employed on a large scale for clean H$_2$ fuel production. Further, this approach seems quite general and should have applications in the preparation of a wide series of TMPs other than MoP and CoP and can be easily integrated with other substrates, such as a photocatalytic layer, for solar fuel production.

ASSOCIATED CONTENT

ⓢ Supporting Information

The Supporting Information is available free of charge on the ACS Publications website at DOI: 10.1021/jacs.6b08491.

> Experimental and theoretical calculation details, instrumentation used, and supplementary figures and tables (PDF)

AUTHOR INFORMATION

Corresponding Authors
*hjliu@rcees.ac.cn
*jhli@mail.tsinghua.edu.cn
Notes
The authors declare no competing financial interest.

REFERENCES

(1) Staszak-Jirkovsky, J.; Malliakas, C. D.; Lopes, P. P.; Danilovic, N.; Kota, S. S.; Chang, K.-C.; Genorio, B.; Strmcnik, D.; Stamenkovic, V. R.; Kanatzidis, M. G.; Markovic, N. M. *Nat. Mater.* **2016**, *15*, 197.
(2) Li, H.; Tsai, C.; Koh, A. L.; Cai, L.; Contryman, A. W.; Fragapane, A. H.; Zhao, J.; Han, H. S.; Manoharan, H. C.; Abild-Pedersen, F.; Norskov, J. K.; Zheng, X. *Nat. Mater.* **2016**, *15*, 48.

(3) Sheng, W.; Gasteiger, H. A.; Shao-Horn, Y. *J. Electrochem. Soc.* **2010**, *157*, B1529.

(4) McCrory, C. C. L.; Jung, S.; Peters, J. C.; Jaramillo, T. F. *J. Am. Chem. Soc.* **2013**, *135*, 16977.

(5) Jaramillo, T. F.; Jorgensen, K. P.; Bonde, J.; Nielsen, J. H.; Horch, S.; Chorkendorff, I. *Science* **2007**, *317*, 100.

(6) Song, F.; Schenk, K.; Hu, X. *Energy Environ. Sci.* **2016**, *9*, 473.

(7) Huan, T. N.; Jane, R. T.; Benayad, A.; Guetaz, L.; Tran, P. D.; Artero, V. *Energy Environ. Sci.* **2016**, *9*, 940.

(8) Yang, H.; Zhang, Y.; Hu, F.; Wang, Q. *Nano Lett.* **2015**, *15*, 7616.

(9) Liang, Y.; Liu, Q.; Asiri, A. M.; Sun, X.; Luo, Y. *ACS Catal.* **2014**, *4*, 4065.

(10) Liu, M.; Li, J. *ACS Appl. Mater. Interfaces* **2016**, *8*, 2158.

(11) Laursen, A. B.; Patraju, K. R.; Whitaker, M. J.; Retuerto, M.; Sarkar, T.; Yao, N.; Ramanujachary, K. V.; Greenblatt, M.; Dismukes, G. C. *Energy Environ. Sci.* **2015**, *8*, 1027.

(12) Liu, P.; Rodriguez, J. A. *J. Am. Chem. Soc.* **2005**, *127*, 14871.

(13) Liu, P.; Rodriguez, J. A.; Asakura, T.; Gomes, J.; Nakamura, K. *J. Phys. Chem. B* **2005**, *109*, 4575.

(14) Ryu, J.; Jung, N.; Jang, J. H.; Kim, H.-J.; Yoo, S. J. *ACS Catal.* **2015**, *5*, 4066.

(15) Xu, K.; Chen, P.; Li, X.; Tong, Y.; Ding, H.; Wu, X.; Chu, W.; Peng, Z.; Wu, C.; Xie, Y. *J. Am. Chem. Soc.* **2015**, *137*, 4119.

(16) Shi, J. P.; Ma, D. L.; Zhang, Y. F.; Liu, Z. F. *Huaxue Xuebao* **2015**, *73*, 877.

(17) Zhang, Y.; Jiang, S.; Song, W.; Zhou, P.; Ji, H.; Ma, W.; Hao, W.; Chen, C.; Zhao, J. *Energy Environ. Sci.* **2015**, *8*, 1231.

(18) Li, J.; Wang, Y.; Zhou, T.; Zhang, H.; Sun, X.; Tang, J.; Zhang, L.; Al-Enizi, A. M.; Yang, Z.; Zheng, G. *J. Am. Chem. Soc.* **2015**, *137*, 14305.

(19) Xie, J.; Zhang, J.; Li, S.; Grote, F.; Zhang, X.; Zhang, H.; Wang, R.; Lei, Y.; Pan, B.; Xie, Y. *J. Am. Chem. Soc.* **2013**, *135*, 17881.

(20) Chen, S.; Duan, J. J.; Ran, J. R.; Jaroniec, M.; Qiao, S. Z. *Energy Environ. Sci.* **2013**, *6*, 3693.

(21) Wang, D.-Y.; Gong, M.; Chou, H.-L.; Pan, C.-J.; Chen, H.-A.; Wu, Y.; Lin, M.-C.; Guan, M.; Yang, J.; Chen, C.-W.; Wang, Y.-L.; Hwang, B.-J.; Chen, C.-C.; Dai, H. *J. Am. Chem. Soc.* **2015**, *137*, 1587.

(22) Wu, H. B.; Xia, B. Y.; Yu, L.; Yu, X.-Y.; Lou, X. W. *Nat. Commun.* **2015**, *6*, 6512.

(23) Lukowski, M. A.; Daniel, A. S.; Meng, F.; Forticaux, A.; Li, L.; Jin, S. *J. Am. Chem. Soc.* **2013**, *135*, 10274.

(24) Chen, W. F.; Wang, C. H.; Sasaki, K.; Marinkovic, N.; Xu, W.; Muckerman, J. T.; Zhu, Y.; Adzic, R. R. *Energy Environ. Sci.* **2013**, *6*, 943.

(25) Liao, L.; Wang, S.; Xiao, J.; Bian, X.; Zhang, Y.; Scanlon, M. D.; Hu, X.; Tang, Y.; Liu, B.; Girault, H. H. *Energy Environ. Sci.* **2014**, *7*, 387.

(26) Song, F.; Hu, X. L. *J. Am. Chem. Soc.* **2014**, *136*, 16481.

(27) Li, J. S.; Wang, Y.; Liu, C. H.; Li, S. L.; Wang, Y. G.; Dong, L. Z.; Dai, Z. H.; Li, Y. F.; Lan, Y. Q. *Nat. Commun.* **2016**, *7*.

(28) Lin, H. L.; Shi, Z. P.; He, S. N.; Yu, X.; Wang, S. N.; Gao, Q. S.; Tang, Y. *Chem. Sci.* **2016**, *7*, 3399.

(29) You, B.; Jiang, N.; Sheng, M.; Gul, S.; Yano, J.; Sun, Y. *Chem. Mater.* **2015**, *27*, 7636.

(30) Hou, C.-C.; Cao, S.; Fu, W.-F.; Chen, Y. *ACS Appl. Mater. Interfaces* **2015**, *7*, 28412.

(31) Vatamanu, J.; Vatamanu, M.; Bedrov, D. *ACS Nano* **2015**, *9*, 5999.

(32) Görlin, M.; Chernev, P.; Ferreira de Araújo, J.; Reier, T.; Dresp, S.; Paul, B.; Krähnert, R.; Dau, H.; Strasser, P. *J. Am. Chem. Soc.* **2016**, *138*, 5603.

(33) Bates, M. K.; Jia, Q.; Doan, H.; Liang, W.; Mukerjee, S. *ACS Catal.* **2016**, *6*, 155.

(34) Liu, Y.; Cheng, H.; Lyu, M.; Fan, S.; Liu, Q.; Zhang, W.; Zhi, Y.; Wang, C.; Xiao, C.; Wei, S.; Ye, B.; Xie, Y. *J. Am. Chem. Soc.* **2014**, *136*, 15670.

(35) Tian, J.; Liu, Q.; Asiri, A. M.; Sun, X. *J. Am. Chem. Soc.* **2014**, *136*, 7587.

(36) Gong, M.; Li, Y.; Wang, H.; Liang, Y.; Wu, J. Z.; Zhou, J.; Wang, J.; Regier, T.; Wei, F.; Dai, H. *J. Am. Chem. Soc.* **2013**, *135*, 8452.

(37) Wang, S.; Pan, L.; Song, J.-J.; Mi, W.; Zou, J.-J.; Wang, L.; Zhang, X. *J. Am. Chem. Soc.* **2015**, *137*, 2975.

(38) Schulthess, T. C.; Temmerman, W. M.; Szotek, Z.; Butler, W. H.; Stocks, G. M. *Nat. Mater.* **2005**, *4*, 838.

(39) Hu, B.; Mai, L.; Chen, W.; Yang, F. *ACS Nano* **2009**, *3*, 478.

(40) Biaso, F.; Burlat, B.; Guigliarelli, B. *Inorg. Chem.* **2012**, *51*, 3409.

(41) Astashkin, A. V.; Rajapakshe, A.; Cornelison, M. J.; Johnson-Winters, K.; Enemark, J. H. *J. Phys. Chem. B* **2012**, *116*, 1942.

(42) Baran, R.; Averseng, F.; Millot, Y.; Onfroy, T.; Casale, S.; Dzwigaj, S. *J. Phys. Chem. C* **2014**, *118*, 4143.

(43) Feng, J.; Sun, X.; Wu, C.; Peng, L.; Lin, C.; Hu, S.; Yang, J.; Xie, Y. *J. Am. Chem. Soc.* **2011**, *133*, 17832.

(44) Lin, C.; Zhu, X.; Feng, J.; Wu, C.; Hu, S.; Peng, J.; Guo, Y.; Peng, L.; Zhao, J.; Huang, J.; Yang, J.; Xie, Y. *J. Am. Chem. Soc.* **2013**, *135*, 5144.

(45) Greeley, J.; Jaramillo, T. F.; Bonde, J.; Chorkendorff, I. B.; Norskov, J. K. *Nat. Mater.* **2006**, *5*, 909.

(46) Gao, M.-R.; Liang, J.-X.; Zheng, Y.-R.; Xu, Y.-F.; Jiang, J.; Gao, Q.; Li, J.; Yu, S.-H. *Nat. Commun.* **2015**, *6*, 5982.

(47) Gerken, J. B.; McAlpin, J. G.; Chen, J. Y. C.; Rigsby, M. L.; Casey, W. H.; Britt, R. D.; Stahl, S. S. *J. Am. Chem. Soc.* **2011**, *133*, 14431.

(48) You, B.; Jiang, N.; Sheng, M.; Bhushan, M. W.; Sun, Y. *ACS Catal.* **2016**, *6*, 714.

(49) Liang, Y.; Wang, H.; Diao, P.; Chang, W.; Hong, G.; Li, Y.; Gong, M.; Xie, L.; Zhou, J.; Wang, J.; Regier, T. Z.; Wei, F.; Dai, H. *J. Am. Chem. Soc.* **2012**, *134*, 15849.

(50) Zhang, M.; de Respinis, M.; Frei, H. *Nat. Chem.* **2014**, *6*, 362.

(51) Wang, X.-D.; Xu, Y.-F.; Rao, H.-S.; Xu, W.-J.; Chen, H.-Y.; Zhang, W.-X.; Kuang, D.-B.; Su, C. *Energy Environ. Sci.* **2016**, *9*, 1468.

(52) Jin, H.; Wang, J.; Su, D.; Wei, Z.; Pang, Z.; Wang, Y. *J. Am. Chem. Soc.* **2015**, *137*, 2688.

(53) Lai, J.; Li, S.; Wu, F.; Saqib, M.; Luque, R.; Xu, G. *Energy Environ. Sci.* **2016**, *9*, 1210.